



Single-atom Ir and Ru anchored on graphitic carbon nitride for efficient and stable electrocatalytic/photocatalytic hydrogen evolution

Zhipeng Yu^{a,b,c,1}, Yifan Li^{d,1}, André Torres-Pinto^{b,c,1}, Alec P. LaGrow^a, Vlad Martin Diaconescu^e, Laura Simonelli^e, Maria J. Sampaio^{b,c}, Oleksandr Bondarchuk^a, Isilda Amorim^{a,f}, Ana Araujo^{a,b,c}, Adrián M.T. Silva^{b,c}, Cláudia G. Silva^{b,c}, Joaquim L. Faria^{b,c,*}, Lifeng Liu^{a,**}

^a Clean Energy Cluster, International Iberian Nanotechnology Laboratory (INL), Avenida Mestre Jose Veiga, 4715-330 Braga, Portugal

^b LSRE-LCM – Laboratory of Separation and Reaction Engineering – Laboratory of Catalysis and Materials, Faculty of Engineering, University of Porto, Rua Dr. Roberto Frias s/n, 4200-465 Porto, Portugal

^c ALiCE – Associate Laboratory in Chemical Engineering, Faculty of Engineering, University of Porto, Rua Dr. Roberto Frias s/n, 4200-465 Porto, Portugal

^d School of Environmental and Municipal Engineering, Qingdao University of Technology, Qingdao 266033, PR China

^e ALBA Synchrotron, Carrer Llum 2-26, Cerdanyola Valles, Barcelona 08290, Spain

^f Centre of Chemistry, Chemistry Department, University of Minho, Campus of Gualtar, Braga 4710-057, Portugal

ARTICLE INFO

Keywords:

Single-atom catalysts
Iridium
Ruthenium
Electrocatalysis
Photocatalysis
Hydrogen evolution reaction

ABSTRACT

Renewable energy-powered water electrolysis and photocatalytic water splitting are two promising approaches to green hydrogen production. Electrocatalysts and photocatalysts are essential components determining the performance of water electrolyzers and photocatalytic reactors, respectively. Currently, there is a pressing need to develop efficient and stable electrocatalysts and photocatalysts for large-scale deployment of these devices to reach carbon neutrality. Herein, we report the synthesis of single-atom Ir and Ru anchored on mesoporous graphitic carbon nitride (Ir-g-CN and Ru-g-CN), which can be used as electrocatalysts and photocatalysts for the hydrogen evolution reaction (HER). Remarkably, Ru-g-CN shows a high turnover frequency (TOF) of 12.9 and 5.1 s⁻¹ at an overpotential (η) of 100 mV in 0.5 M H₂SO₄ and 1.0 M KOH, respectively, outperforming Ir-g-CN, commercial Pt/C benchmark and many other advanced HER catalysts reported recently. Moreover, Ru-g-CN can deliver an exceptionally high mass activity of 24.55 and 8.78 A mg⁻¹ at η = 100 mV in acidic and alkaline solutions, meanwhile exhibiting a high apparent current density, which is favorable for practical applications. Additionally, both Ru-g-CN and Ir-g-CN show outstanding catalytic stability, continuously catalyzing the HER in acidic and alkaline conditions for 120 h with minimal degradation. Besides, when used for photocatalytic water splitting, Ru-g-CN can achieve a high hydrogen production rate of 489.7 mmol H₂ g_{Ru}⁻¹ h⁻¹, and shows good photocatalytic stability. Our density functional theory (DFT) calculations demonstrate that loading Ir and Ru single-atoms on g-CN alters the electronic structure, resulting in a reduced bandgap and improved electrical conductivity, facilitating electron transfer during the catalysis. Moreover, the Gibbs free energy of hydrogen adsorption on Ru-g-CN and Ir-g-CN is also substantially lowered, enhancing HER performance.

1. Introduction

Hydrogen (H₂), as a carbon-free energy carrier with a high gravimetric energy density, has shown significant potential for decarbonizing the transport sector and hard-to-abate industries [1], contributing to

reaching the carbon-neutral goals pledged by many countries in the world. Water electrolysis coupled with renewable sources [2–4] and direct solar-driven photocatalysis [5–8] have been considered the most promising approaches to “green” H₂ production. To turn the blueprint into reality, water electrolyzers and photocatalytic reactors must be

* Correspondence to: Clean Energy Cluster, International Iberian Nanotechnology Laboratory (INL), Portugal.

** Corresponding author.

E-mail addresses: jlfaria@fe.up.pt (J.L. Faria), lifeng.liu@inl.int (L. Liu).

¹ Zhipeng Yu, Yifan Li and André Torres-Pinto contributed equally to this work.

deployed on a large scale commensurate with the global demand. Given that hydrogen evolution reaction (HER) catalysts and photocatalysts are crucial components governing the performance of electrochemical and photocatalytic water splitting, respectively, there is a pressing need to develop efficient, stable and cost-effective HER electrocatalysts and photocatalysts to enable fast, widespread deployment of water electrolyzers and photocatalytic reactors across different sectors where H_2 is needed.

Since its report in 2009 [9], graphitic carbon nitride (g-CN) has been intensively investigated as a metal-free photocatalyst for H_2 production [5,6,10,11]. Despite being active, the H_2 production rate of pure g-CN is, in general, not sufficiently high, and it was demonstrated that loading co-catalysts on g-CN can markedly enhance the H_2 evolution performance [3,12]. Besides, g-CN was also explored as an electrocatalyst for electrochemical water splitting [13]. However, g-CN is a polymer semiconductor having a bandgap of ~ 2.7 eV. It has poor electrical conductivity, and therefore pure g-CN by nature is not a suitable electrocatalyst [13]. Nevertheless, recent theoretical studies and experimental investigations have demonstrated that g-CN loaded with noble or transition metal species can serve as an outstanding electrocatalyst toward the HER in acidic and alkaline electrolytes [14–16]. For example, Zheng et al. reported that anomalous face-centered cubic (fcc) Ru nanoparticles supported on g-CN exhibited 2.5 times higher hydrogen evolution turnover frequency (TOF) under alkaline conditions than the state-of-the-art commercial Pt/C catalysts [15], which can be attributed to the favorable water dissociation dictated by the combination of Ru and g-CN. In particular, metal species atomically dispersed on the surface of g-CN have recently emerged as a new class of electrocatalysts, which can optimize the utilization of metals, especially the costly platinum group metals (PGMs), and also enable notably improved catalytic performance [12,17–21]. To this end, g-CN emerges as an excellent supporting material because of its abundant uncoordinated nitrogen groups that can firmly anchor metal species, resulting in improved atomic dispersion [13].

Recent density functional theory (DFT) calculations revealed that introducing single metal (M) atoms onto the surface of g-CN may remarkably lower the bandgap [22], improving the conductivity of the resulting M-g-CN. Moreover, this will cause a drastic change in the electronic structure and alter the ratio of ionic to covalent bonding, thereby changing the adsorption energy of intermediates, the free energy of hydrogen adsorption and accordingly, the HER overpotential [17,18]. Experimentally, M-g-CN has recently been demonstrated to be active for both electrochemical and photocatalytic water splitting. For instance, Peng et al. reported that Ru ion-complexed g-CN nanosheets could catalyze the HER with an overpotential (η) of 140 mV to achieve a current density of 10 mA cm^{-2} and a Tafel slope of 57 mV dec^{-1} [23]. Liu and co-workers lately demonstrated that by introducing only 0.1 wt % of palladium clusters and single-atoms on g-CN, the photocatalytic H_2 production rate of g-CN could increase from 1.4 to $728 \mu\text{mol g}^{-1} \text{ h}^{-1}$ under visible light irradiation [24]. Notwithstanding some progress, most of the previous reports were mainly focused on g-CN supported Pt single-atom catalysts [12,13]; moreover, the electrocatalytic and photocatalytic properties of M-g-CN toward hydrogen evolution were usually investigated separately. More importantly, both the electrocatalytic and photocatalytic performance of these catalysts need to be further improved to explore possible synergies between the processes.

This work reports the synthesis of single-atom Ir and Ru anchored on mesoporous g-CN (denoted as Ir-g-CN and Ru-g-CN) by a simple hydrothermal method. Both Ir-g-CN and Ru-g-CN are comprehensively characterized, and the dispersion of Ir and Ru species on the g-CN support is evidenced by advanced scanning transmission electron microscopy. The obtained Ir-g-CN and Ru-g-CN show outstanding electrocatalytic performance for HER. Notably, the Ru-g-CN exhibits a high TOF value of 12.9 and 5.1 s^{-1} at $\eta = 100$ mV in 0.5 M H_2SO_4 and 1.0 M KOH, respectively, which outperforms Ir-g-CN, commercial Pt/C benchmark and many other advanced HER catalysts recently reported in

the literature. In addition, Ru-g-CN affords an exceptionally high mass activity of 24.55 and 8.78 A mg^{-1} at $\eta = 100$ mV in acidic and alkaline solutions, meanwhile exhibiting a high apparent current density, which is favorable for practical applications. Impressively, Ru-g-CN also reveals outstanding photocatalytic HER activity showing a high H_2 production rate of $489.7 \text{ mmol H}_2 \text{ g}_{\text{Ru}}^{-1} \text{ h}^{-1}$, along with good catalytic stability. Our DFT calculations disclose that the atomic dispersion of Ir and Ru on g-CN reduces the bandgap and increases electrical conductivity. Moreover, DFT results can also explain the improved HER activity through the lowering of the Gibbs free energy of hydrogen adsorption on Ir-g-CN and Ru-g-CN.

2. Experimental section

2.1. Reagents

Dicyandiamide (99 wt%), ethylene glycol (EG), iridium chloride hydrate ($\text{IrCl}_3 \cdot x\text{H}_2\text{O}$) and Nafion® perfluorinated resin solution (5 wt%) were purchased from Sigma-Aldrich. Ruthenium chloride hydrate ($\text{RuCl}_3 \cdot x\text{H}_2\text{O}$) and commercial Pt/C (20 wt%) were acquired from Johnson Matthey. All reagents were used as received without further purification.

2.2. Synthesis of Ir-g-CN and Ru-g-CN

Firstly, the mesoporous g-CN was synthesized by a simple thermal decomposition process of dicyandiamide under a static air atmosphere at 550°C , using a Phoenix Microwave Muffle Furnace (CEM Corporation) according to the pre-established thermal muffle furnace procedure [25]. The resulting solids were ground and washed, followed by filtration, and dried overnight at 120°C . The obtained powders were then collected and loaded in an open crucible, calcined in air at 500°C for 2 h. The as-prepared product is labeled as g-CN. In the synthesis of Ir-g-CN and Ru-g-CN, 100 mg of g-CN was added to 16 mL of EG, followed by ultrasonication for 1 h to obtain a homogeneous solution. Subsequently, 4 mL of 2 mg L^{-1} IrCl_3/EG or RuCl_3/EG mixture was added to the g-CN/EG solution, and the solution was then mixed homogeneously by ultrasonication. Afterward, the solution was continuously stirred for 12 h to disperse the Ir or Ru precursors into the mesoporous g-CN adequately. In the next step, the mixed solution was transferred into a Teflon-lined stainless steel autoclave reactor, heated to 130°C , and maintained at this temperature for 3 h. After the reactor was naturally cooled down to 25°C , the obtained precipitates were centrifuged, washed twice with deionized water and ethanol sequentially, and then dried under vacuum at 60°C for further use.

2.3. Materials characterization

Scanning electron microscopy (SEM) was performed on an FEI Quanta 650 FEG microscope. The high-angle annular dark-field scanning transmission electron microscopy (HAADF-STEM) was carried out on an image- and probe-corrected transmission electron microscope operating at 200 kV (FEI Themis 60–300). X-ray diffractometry (XRD) examination was conducted on an X'Pert PRO diffractometer (PANalytical) set at 45 kV and 40 mA, using Cu K_α radiation ($\lambda = 1.5406 \text{ \AA}$) and a PIXcel detector. Experimental data were obtained with the Bragg-Brentano configuration in the 2θ range of $10 - 90^\circ$ at a scan speed of $0.011^\circ \text{ s}^{-1}$. Fourier transform infrared spectroscopy (FT-IR) was performed on an ERTEX 80 v vacuum FT-IR spectrometer (Bruker). Nitrogen adsorption/desorption porosimetry measurements were conducted at 77 K using a Quantachrome Autosorb IQ₂ system, and the surface area of samples was derived by the Brunauer-Emmett-Teller (BET) method. X-ray photoelectron spectroscopy (XPS) experiments were carried out on an ESCALAB 250 instrument with Al K_α X-rays (1486.6 eV), and ultraviolet photoelectron spectroscopy (UPS) measurements were conducted with an unfiltered He I (21.22 eV) gas discharge lamp to

calculate the valence band maximum (VBM). The loading mass of Ir and Ru on g-CN was determined by the inductively coupled plasma – optical emission spectroscopy (ICP-OES, ICPE-9000 spectrometer, Shimadzu). The Diffuse Reflectance Ultraviolet-Visible (DR UV-vis) spectra were recorded on a UV-vis spectrophotometer (Jasco V-560) equipped with an integrating sphere attachment (Jasco ISV-469), with data being converted to equivalent absorption Kubelka-Munk units to construct the respective Tauc plot. Photoluminescence (PL) spectra were acquired between 400 and 650 nm, using a spectrofluorometer (Jasco FP-8300) with a 150 W Xenon lamp under 370 nm excitation while fixing the emission and excitation bandwidths at 2.5 nm. The X-ray absorption spectroscopy (XAS) experiments were carried out at the CLAES beamline of the ALBA Synchrotron [26]. Samples were prepared as solid pellets diluted in cellulose. Data were acquired at room temperature using a Si311 double crystal monochromator. Ir L₃-edge spectra were collected in transmission mode, while Ru K-edge was measured in transmission for the references and in fluorescence mode for the catalyst by means of a multi-channel SDD detector. Several XAS repeats were made to ensure reproducibility and statistics. The averaged spectra were treated with the Athena software package [27]. The energy scale was calibrated by setting the first inflection point of Pt foil to 11,564 eV in the case of Ir data and to the first inflection point of RuO₂ taken as 22,129 eV for Ru data.

2.4. Electrocatalytic tests

The electrocatalytic experiments were performed in a three-electrode configuration at room temperature using a Biologic VMP-3 potentiostat/galvanostat. The catalyst ink was prepared by ultrasonically dispersing 5 mg of Ir-g-CN and Ru-g-CN catalysts into 500 μ L of isopropanol + 50 μ L of Nafion® (Sigma, 5 wt%) solution. Afterward, 13.2 μ L of catalyst ink was evenly drop-cast on the glassy carbon (GC) electrode with an exposed area of 0.2 cm². For comparison, the commercial Pt/C (20 wt%, Johnson Matthey) catalysts and g-CN support as control samples were also investigated. The catalyst-loaded GC, a graphitic rod, and a saturated calomel electrode (SCE) were used, respectively, as the working, counter, and reference electrodes. All potentials are converted to the reversible hydrogen electrode (RHE) scale according to the following formula:

$$E_{\text{RHE}} = E_{\text{SCE}} + 0.059 \times \text{pH} + 0.241 \quad (1)$$

Cyclic voltammetry (CV) was carried out at a scan rate of 5 mV s⁻¹ to evaluate the apparent HER activity of catalysts, and an *iR*-correction (85%) was made to compensate for the voltage drop between the reference and working electrodes. The electrochemical double-layer capacitance (*C_{dl}*) was measured to calculate the catalysts' electrochemically active surface area (ECSA). The *C_{dl}* value of catalysts was estimated by performing CV in the non-Faradaic potential range of 0.32–0.52 V vs. RHE in 1.0 M KOH at different scan rates (*v*) of 10, 20, 30, 40, 50, 60, 70, 80, 90 and 100 mV s⁻¹, followed by extracting the slope from the resulting $|j_a - j_c|/2$ vs. *v* plots, where *j_a* and *j_c* represent the anodic and cathodic currents obtained at 0.42 V vs. RHE, respectively. The ECSA was estimated upon dividing *C_{dl}* by the capacitance of a model catalyst over a unit surface area (usually 0.035 mF cm⁻² for noble metals) [28,29], as follows:

$$\text{ECSA} = C_{\text{dl}} / 0.035 \text{ mF cm}^{-2} \quad (2)$$

Furthermore, the TOF values were calculated through the following equation [30]:

$$\text{TOF} = \frac{j}{2nF} \quad (3)$$

where *j* (A) is the current at a given overpotential, *F* = 96,500 C mol⁻¹ stands for the Faraday constant, and *n* (mol) represents the mole number of Ir or Ru loaded on the g-CN support calculated from the ICP-OES

measurements. All metal species in catalysts are assumed to be catalytically active, so the calculated values represent the lower limit of TOF.

Electrochemical impedance spectroscopy (EIS) tests were performed at -0.075 V vs. RHE in the frequency range of 10⁵ – 0.01 Hz with a 10 mV sinusoidal perturbation. The stability of catalysts was assessed at a constant current density of -10 mA cm⁻² using chronopotentiometry (CP). Mott-Schottky (M-S) plots were acquired in 0.5 M Na₂SO₄ at the frequency of 1000 Hz, where the initial potential, final potential and amplitude of perturbation were set to 0.66 V, 1.5 V vs. RHE and 0.01 V, respectively.

2.5. Photocatalytic tests

The photocatalytic H₂ production tests were carried out at room temperature in a cylindrical glass immersion photo-reactor coupled with a DURAN® glass cooling jacket. The irradiation system consisted of four near-UV light-emitting diodes (LEDs) as the light source (λ_{max} = 417 nm), placed equidistantly at 3.5 cm from the reactor wall. The LED intensity reaching the reactor wall was ca. 450 W m⁻² determined by a spectroradiometer (USB2000 +, Ocean Optics, USA). The reactor was charged with 150 mL of the aqueous solution, containing 75 mg of catalysts and 10% v/v methanol as the sacrificial agent. The suspension was first degassed by a nitrogen flow for 20 min, after which the light was turned on. During measurements, the N₂ flow was maintained at a rate of 10 cm³ min⁻¹. H₂ was detected in-line using an Inficon Micro GC 3000 gas chromatograph equipped with a molecular sieve column and a micro-TCD detector. Argon (Ar) was used as the carrier gas. The photocatalytic durability tests used the same catalysts recycled by filtration, followed by washing and drying, after finishing one photocatalytic cycle and before using them in the next cycle.

2.6. DFT calculations

The first-principles density functional theory (DFT) calculations were performed using Vienna Ab-initio Simulation Package (VASP) with the projector augmented wave (PAW) [31–33]. Since the generalized gradient approximation (GGA) functionals such as Perdew-Burke-Ernzerhof (PBE) tend to underestimate the bandgap of materials, the electronic properties were calculated using the hybrid HSE06 functional [34]. The energy cutoff was set to 450 eV, and the atomic positions were allowed to relax until the energy and force were less than 10⁻⁵ eV and 10⁻² eV Å⁻¹, respectively. The crystal lattices of g-CN used for computation are *a* = 7.13 Å and *b* = 7.13 Å, and a double layer periodic slab of g-CN with a 15 Å separation in the *z*-direction was used to model the experimental work. The Brillouin zone was sampled using 5 × 5 × 1 and 9 × 9 × 1 Monkhorst-Pack *k*-point grid for structure optimization and electronic property calculation, respectively. For Ir-g-CN and Ru-g-CN, the optimized most stable structural models are Ir₁N_x or Ru₁N_x single-site/g-CN, where the Ir or Ru atom is embedded in the plane and forms chemical bonds with two N atoms.

The HER proceeds through two-electron pathways with the following reaction steps:



where M* represents the Ir or Ru active site, and H* is the hydrogen intermediate adsorbed on the active sites during the HER. The adsorption energy was calculated according to the following equation:

$$G_{\text{ad}} = G_{\text{sys}} - G_{\text{sur}} - G_{\text{spe}} \quad (6)$$

where *G_{ad}*, *G_{sys}*, *G_{sur}* and *G_{spe}* denote the adsorption free energy, the free energy of the adsorption system, the free energy of a clean surface and the free energy of the isolated adsorption species, respectively.

3. Results and discussion

3.1. Physicochemical characterization of Ir-g-CN and Ru-g-CN

As detailed in the Experimental section, the Ir-g-CN and Ru-g-CN catalysts were prepared by wet chemical reduction of Ir- and Ru-containing precursors on the mesoporous g-CN support under hydrothermal conditions. g-CN is known to have abundant uncoordinated N groups on its surface [19,20], which can anchor metal cations firmly, leading to a high degree of dispersion of Ir and Ru species. SEM examination showed that the as-prepared g-CN consists of carbon nitride thin layers stacked together into micrometer-sized particles, and loading Ir or Ru on g-CN did not change its morphology (Fig. S1). The aberration-corrected HAADF-STEM was further carried out to investigate the microstructure of Ir-g-CN and Ru-g-CN, where numerous mesopores were found in the g-CN support of both samples (Fig. 1a and d), which are expected to offer high surface areas and enable the exposure of more catalytically active sites. Further HAADF-STEM imaging at higher magnification revealed a high degree of atomic dispersion of Ir and Ru atoms on the g-CN support (See the bright spots in Fig. 1b and e. Some of them are marked with red circles in Fig. 1c and f). While most metal species were found in the form of single-atoms, sparse ultrafine nanoclusters with a subnanometer diameter were also observed in some places of both samples. Elemental mapping over Ir-g-CN and Ru-g-CN further corroborated that Ir or Ru element is distributed relatively uniformly over the g-CN with a high density (Fig. S2b-d and f-h).

The crystal structure and chemical composition of Ir-g-CN and Ru-g-CN catalysts were further investigated by XRD, FT-IR and XPS. According to the XRD results (Fig. 2a), only one strong diffraction peak at 27.6° and another very weak one at 12.9° , which can be assigned to the diffractions of (002) and (100) planes of g-CN, are observed for all samples, and no other diffraction peaks from any polymorphs of Ir, Ru or their compounds can be identified. Therefore, no crystalline structures,

such as big nanoparticles or clusters, are formed when loading Ir or Ru on the g-CN support. As such, Ir or Ru should virtually be atomically dispersed, consistent with the HAADF-STEM examination (Fig. 1). The diffraction intensity of sparsely dispersed subnanometric Ir and Ru clusters (Fig. S2) is not strong enough to show any peaks in the XRD patterns, implying that the quantity of such clusters is insignificant. The FT-IR spectra of Ir-g-CN and Ru-g-CN catalysts closely resemble that of as-prepared g-CN, indicating that introducing Ir and Ru atoms onto g-CN did not alter the bulk molecular structure of the g-CN (Fig. 2b). The BET specific surface area of the Ir-g-CN catalysts was measured to be $64.9 \text{ m}^2 \text{ g}^{-1}$, slightly lower than that of Ru-g-CN ($79.0 \text{ m}^2 \text{ g}^{-1}$), but both are almost two times higher than that of the original g-CN ($34.7 \text{ m}^2 \text{ g}^{-1}$). This increase suggests that loading Ir or Ru atoms onto g-CN remarkably enlarges the specific surface area of samples, which is beneficial for exposing more active sites and promoting mass transport [35].

The surface chemistry of Ir-g-CN and Ru-g-CN was further analyzed by XPS. The XPS survey spectra of samples confirm the presence of corresponding elements in each catalyst, as shown in Fig. S3. The high-resolution N 1s spectra of g-CN, Ir-g-CN and Ru-g-CN are shown in Fig. 2d-f. The N 1s XPS spectrum of g-CN can be deconvoluted into four components (Fig. 2d), corresponding to triazine rings (C–N=C, 398.7 eV), tertiary nitrogen (N–(C)₃, 400.7 eV), amino function groups (401.9 eV) and the nitrate group (404.5 eV) [25], respectively. Compared to the pristine g-CN, Ir-g-CN and Ru-g-CN have one more component appearing at 399.6 eV, which can be assigned to the metal–nitrogen (M–N) bonding [36,37] resulting from the anchoring of Ir and Ru atoms on the g-CN surface. Meanwhile, the C 1s XPS spectra of these samples were also compared. The C 1s XPS spectrum of g-CN is deconvoluted into three components (Fig. S4a), corresponding to the sp^2 -bonded carbon in N-containing aromatic rings (N–C=N, 288.6 eV), amino functional groups (286.3 eV) and C–(N)₃ planar trigonal carbon geometry (284.9 eV) [38]. After loading Ir and Ru onto g-CN, the intensity of N–C=N signals relative to that of the other two components is

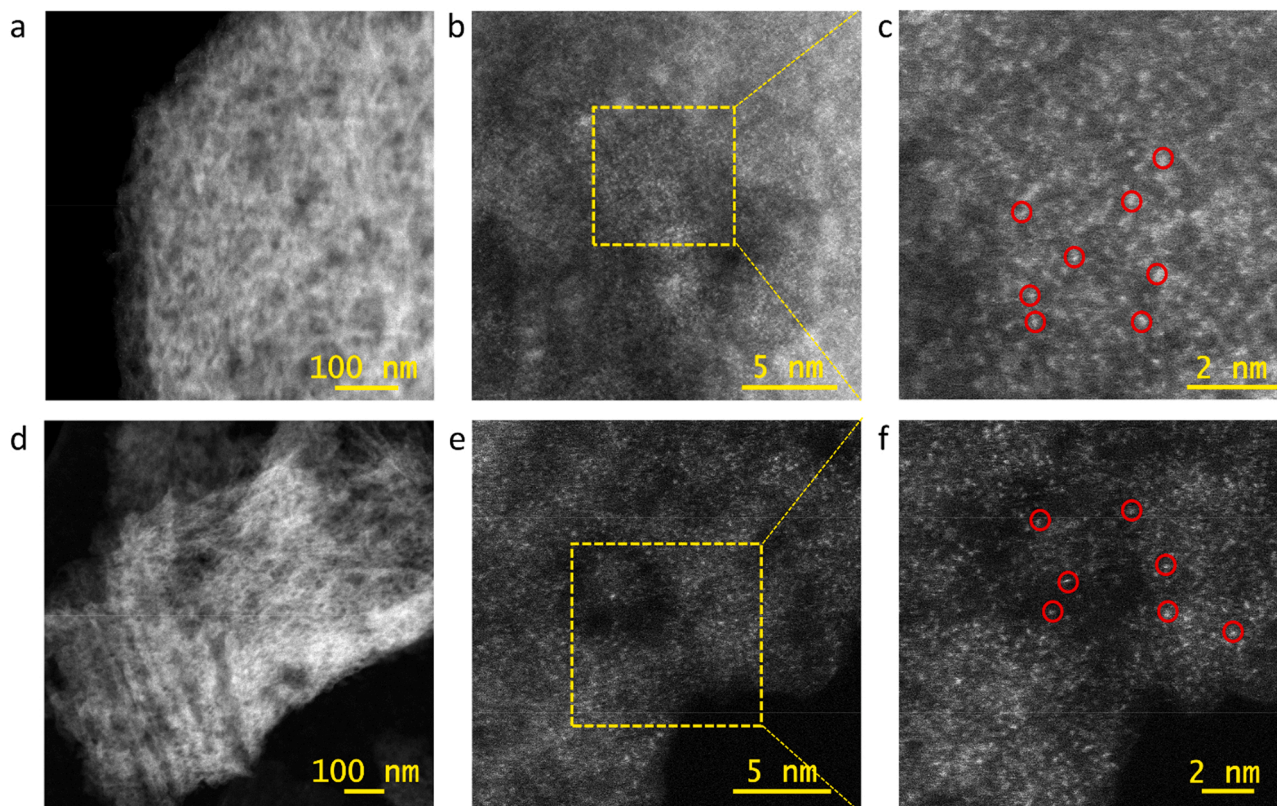


Fig. 1. Aberration-corrected HAADF-STEM images of (a–c) Ir-g-CN and (d–f) Ru-g-CN. Red circles in (c) and (f) spotlight representative Ir and Ru single-atoms, respectively.

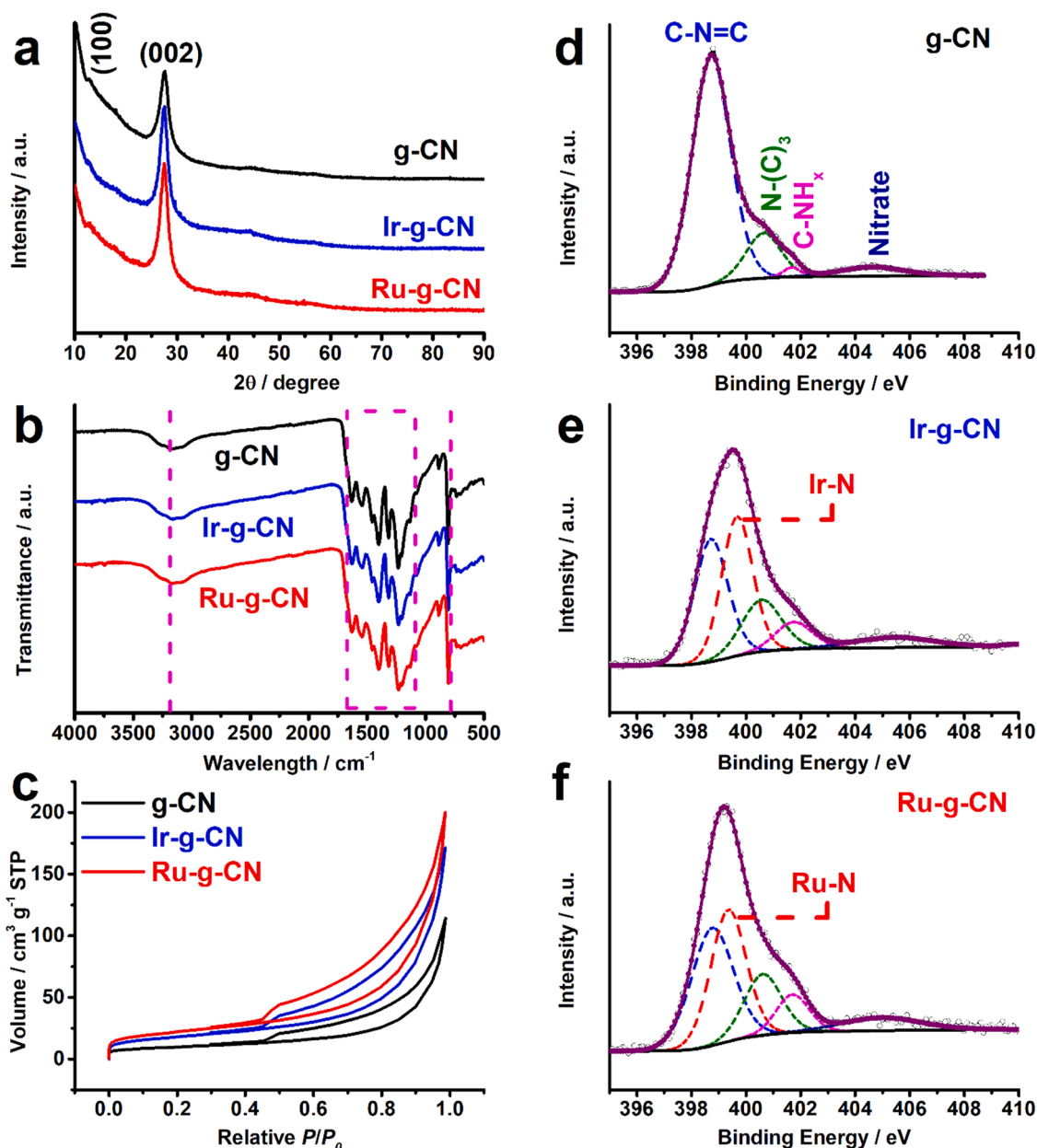


Fig. 2. (a) XRD patterns, (b) FT-IR spectra, (c) Nitrogen adsorption-desorption isotherms of all catalysts. The high-resolution N 1s spectrum of (d) g-CN, (e) Ir-g-CN and (f) Ru-g-CN catalysts.

decreased (Fig. S4b and c), which can be attributed to the N bonding with Ir and Ru species, consistent with the results for N 1s spectra (Fig. 2d-f). In addition, ICP-OES measurements were performed, which revealed that the loading mass of Ir and Ru on g-CN is 1.71 wt% and 0.24 wt% for Ir-g-CN and Ru-g-CN, respectively.

Moreover, X-ray absorption near-edge structure (XANES) spectroscopy measurements were carried out to gain more insight into the chemical state. Fig. S5a shows the Ir L₃-edge XANES spectra of metallic Ir, commercial IrO₂ and Ir-g-CN. The absorption white-line of Ir-g-CN stands in the middle of that of metallic Ir and IrO₂ references, indicating an average Ir oxidation state lower than +4 but higher than 0. This is in good agreement with the XPS results, where no components from metallic Ir⁰ are observed, and the oxidation state of Ir has been found close to 3+ (Fig. S6a). Fig. S5b reveals the Ru K-edge XANES spectra of metallic Ru, commercial RuO₂ and Ru-g-CN, respectively, where the Ru in Ru-g-CN is more reduced than that in RuO₂ (4+) but more oxidized than that in metallic Ru, indicating that the Ru in Ru-g-

CN carries positive charges, consistent with the XPS results (Fig. S6b). The absence of reduced metallic forms in Ir-g-CN and Ru-g-CN implies that Ir and Ru are predominantly dispersed atomically on the g-CN support [39,40], agreeing with the above XRD and HAADF-STEM results.

3.2. Optical properties of Ir-g-CN and Ru-g-CN

g-CN is known to be a polymeric semiconductor [13], and therefore the effect of introducing Ir and Ru co-catalysts on the optical properties of g-CN was further investigated. According to the DR UV-vis spectra measured in the wavelength range of 300–700 nm (Fig. 3a), the light absorption of both Ir-g-CN and Ru-g-CN exhibits an increase over the whole spectral range, accompanied by a slight red shift in the absorption edge with respect to the as-obtained g-CN support. This indicates that the interaction between Ir or Ru atoms and g-CN enhances light absorption, which improves photocatalytic activity [12,41]. Furthermore,

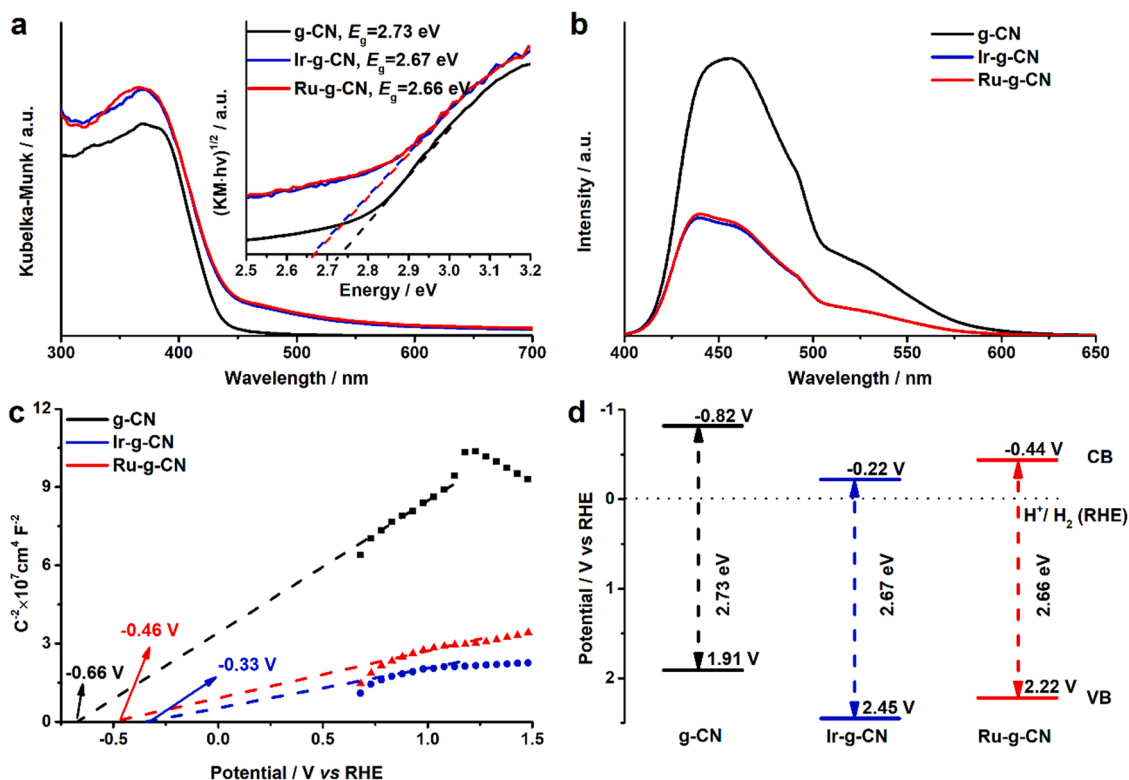


Fig. 3. (a) UV-vis absorption spectra and the corresponding Tauc plots (inset), (b) PL spectra, (c) Mott-Schottky plots and (d) the corresponding electronic band structure of g-CN, Ir-g-CN and Ru-g-CN catalysts.

the optical band gap (E_g) of Ir-g-CN and Ru-g-CN was estimated from the Tauc plot (Fig. 3a inset), which shows a very similar value for Ir-g-CN (2.67 eV) and Ru-g-CN (2.66 eV), slightly lower than that of the as-prepared g-CN (2.73 eV). This was also confirmed by photoluminescence (PL) measurements (Fig. 3b), where the PL signals of Ir-g-CN and Ru-g-CN are significantly lower in comparison with that of g-CN, suggesting that the photo-carrier collection in Ir-g-CN and Ru-g-CN works efficiently and that the incorporation of atomically dispersed Ir or Ru can effectively suppress the electron-hole recombination, promoting the separation and transfer of photo-carriers [11,22,42].

To further investigate the band structure of the Ir-g-CN and Ru-g-CN catalysts, Mott-Schottky analyses were conducted at a frequency of 1000 Hz. All samples show the n-type semiconductor characteristics, with a positive slope in the Mott-Schottky plots (Fig. 3c). The flat band potentials of g-CN, Ir-g-CN and Ru-g-CN can be extrapolated to be -0.66 V, -0.33 V and -0.46 V vs. RHE, respectively [43]. Considering the energy gap (E_g) between the Fermi level (E_F) and the valence band maximum (E_v) of different samples obtained by the UPS-VBM spectrum (Fig. S7), the valence band position (E_v) and conduction band position (E_c) could be estimated [42] (Fig. 3d and Table S1). Since the conduction band of Ir-g-CN and Ru-g-CN is much closer to the Fermi level than that of the original g-CN, the Ir or Ru atoms serve as electron acceptors. In this case, the electron transfer from the support to Ir or Ru co-catalysts will be promoted under photo-irradiation, and thus the electron-hole recombination can be effectively suppressed [11].

3.3. Electrocatalytic performance of Ir-g-CN and Ru-g-CN

The electrocatalytic HER activities of Ir-g-CN and Ru-g-CN catalysts were investigated by linear sweep voltammetry (LSV) in both 0.5 M H_2SO_4 and 1.0 M KOH solutions. Pristine g-CN and commercial 20% Pt/C catalysts were used as references. Fig. 4a and b show that the pristine g-CN support exhibits inferior HER performance in acidic and

alkaline solutions. Upon loading a tiny amount of Ir or Ru (1.71 wt% for Ir-g-CN and 0.24 wt% for Ru-g-CN), the apparent HER activity is significantly enhanced in both cases, even outperforming the commercial Pt/C benchmark, particularly in the low overpotential (η) region. This performance indicates that dispersing Ir or Ru in the form of single-atoms is an effective strategy to reduce the utilization of precious metals while retaining adequately sound HER performance. The flat portion of LSV curve for Pt/C might result from the hydrogen buildup at low overpotentials, which is likely related to the mass-transport limitations, according to a recent report [44]. The reaction kinetics of all catalysts was studied by the Tafel analysis (Fig. S8a and b). The Ir-g-CN and Ru-g-CN catalysts exhibit a Tafel slope of 47.6 and 54.0 mV dec^{-1} , respectively, in 0.5 M H_2SO_4 , slightly higher than that of commercial Pt/C (32.2 mV dec^{-1}), indicating that the HER proceeds on Ir-g-CN and Ru-g-CN through the Volmer-Heyrovsky mechanism, where the electrochemical desorption is fast, but the discharge step is slow. In 1.0 M KOH, the Ir-g-CN shows a Tafel slope of 49.3 mV dec^{-1} , followed by commercial Pt/C (61.0 mV dec^{-1}) and Ru-g-CN (63.5 mV dec^{-1}), suggesting more favorable HER kinetics on Ir-g-CN. Furthermore, the EIS measurements also confirmed the fast reaction rate of the Ir-g-CN and Ru-g-CN for the HER, as evidenced by their small charge transfer resistance (R_{ct} , Fig. S8c and d).

To further assess the intrinsic catalytic performance, the ECSAs of Ir-g-CN, Ru-g-CN and reference catalysts were estimated and compared through the electrochemical double-layer capacitance (C_{dl}) measurements [28]. As revealed in Fig. S9, Ir-g-CN shows an ECSA value of 234.3 cm^2 , higher than the commercial Pt/C (227.1 cm^2) and Ru-g-CN (114.0 cm^2). The ECSA normalized specific activity of Ru-g-CN outperforms that of Ir-g-CN and Pt/C in both acidic and alkaline electrolytes (Fig. S10), indicating the intrinsically high HER activity of Ru-g-CN. Furthermore, the TOF values of Ir-g-CN and Ru-g-CN were also calculated and compared to those of other advanced Ir- and Ru-based HER electrocatalysts reported recently (Fig. S11). The Ru-g-CN shows a TOF value of 12.9 and 5.1 s^{-1} at $\eta = 100$ mV in 0.5 M H_2SO_4 and 1.0 M KOH,

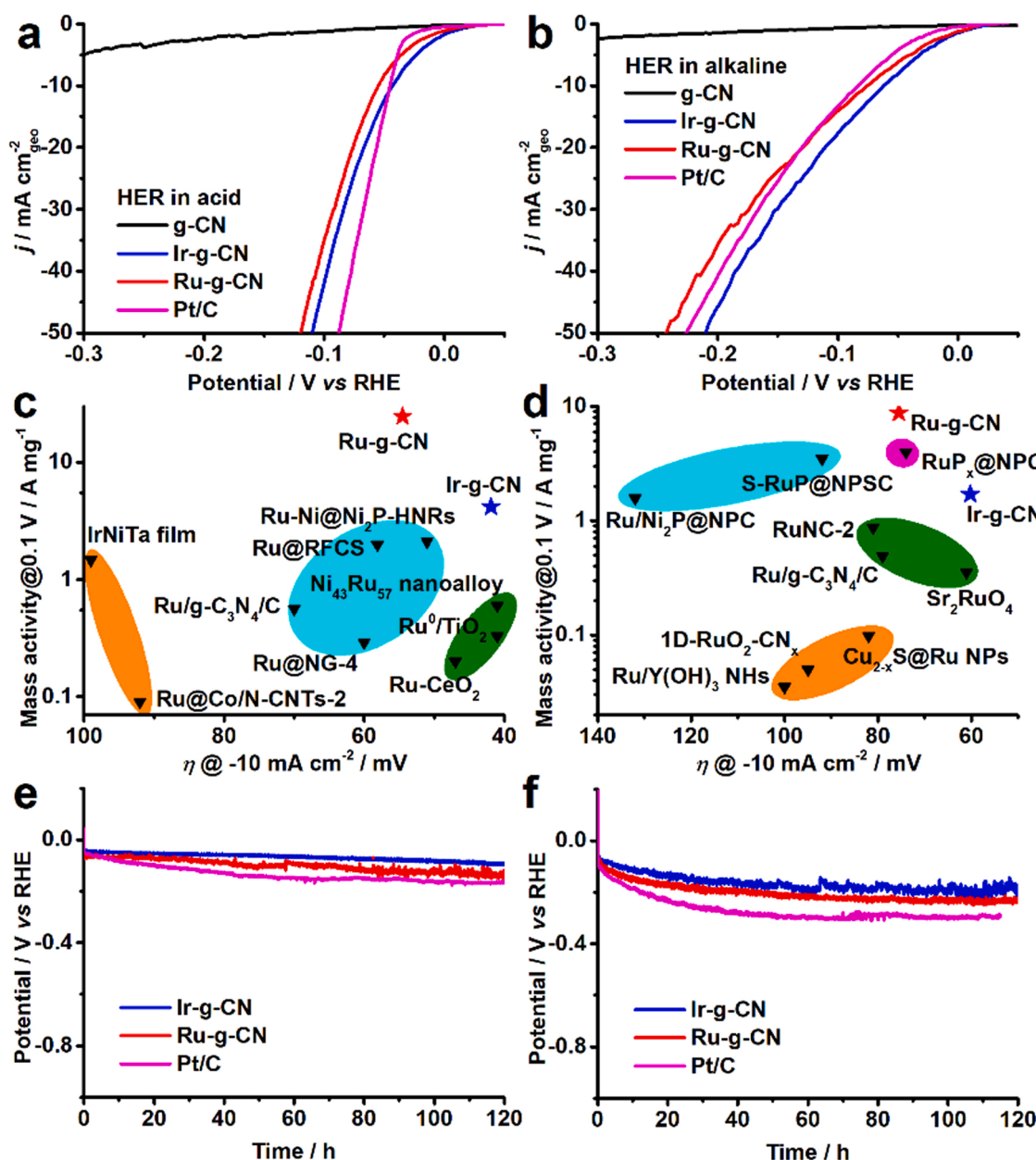


Fig. 4. Electrocatalytic HER performance of g-CN, Ir-g-CN and Ru-g-CN catalysts. (a, b) LSV curves. Scan rate: 5 mV s⁻¹. (c, d) Comprehensive comparison of the mass activity versus apparent activity of Ir-g-CN and Ru-g-CN to those of other start-of-the-art Ir- and Ru-based catalysts reported recently. See [Supporting Information](#) for details. (e, f) Long-term catalytic stability tests at -10 mA cm^{-2} . Data were acquired in (a, c, e) 0.5 M H₂SO₄ and (b, d, f) 1.0 M KOH, respectively.

respectively, substantially outperforming commercial Pt/C and many other Ir-/Ru-based electrocatalysts (Tables S2 and S3), such as Ru/g-C₃N₄/C (4.85 s⁻¹ at $\eta = 100 \text{ mV}$ in acid) [15], RuCoP (10.95 s⁻¹ at $\eta = 100 \text{ mV}$ in acid) [45], and np-Cu₅₃Ru₄₇ (1.139 s⁻¹ at $\eta = 100 \text{ mV}$ in alkaline) [46].

For PGM electrocatalysts, both mass activity and apparent activity are crucial metrics for practical applications in electrolyzers [21,29]. For single-atom catalysts, the low metal loading would lead to a high normalized mass activity, but this advantage in many cases cannot be fully translated into practical applications. For catalysts with a relatively low PGM loading density, the catalyst layer must be thick enough to deliver a given high catalytic current (not current density), which would hinder efficient mass and charge transport within the electrode, eventually compromising the overall catalytic performance of the electrode. Therefore, a more comprehensive assessment considering both mass and apparent activities is critically needed, especially for single-atom

catalysts. To this end, the mass activity of Ru-g-CN at $\eta = 100 \text{ mV}$ versus its apparent activity at -10 mA cm^{-2} is plotted and compared to that of other advanced Ru-based electrocatalysts reported recently. Ru-g-CN can deliver an exceptionally high mass activity of 24.55 and 8.78 A mg⁻¹ at $\eta = 100 \text{ mV}$ in 0.5 M H₂SO₄ and 1.0 M KOH, respectively, and meanwhile afford an apparent current density of -10 mA cm^{-2} at a low overpotential (positioned in the upper right corner in Fig. 4c and d), outperforming many other catalysts tested under the same conditions (Tables S4 and S5). In addition, the Faradaic efficiency of Ir-g-CN and Ru-g-CN toward the HER was measured (Fig. S12), and the volume of H₂ gases collected matches well with that calculated, indicating a near 100% Faradaic efficiency.

The electrocatalytic stability is another significant performance indicator of an HER catalyst in practical applications. The commercial Pt/C catalysts display a gradually decreased activity upon continuous HER electrolysis at -10 mA cm^{-2} for 120 h in both acidic and alkaline

solutions (Fig. 4e and f), in agreement with previous reports [45,47], which likely results from the weak binding between Pt nanoparticles and the carbon support. In contrast, although Ir-g-CN and Ru-g-CN also exhibit slow degradation in HER activity, this happens to a much lesser extent compared to the commercial Pt/C catalysts, which may originate from the strong chemical bonding between Ir/Ru atoms and uncoordinated N in g-CN that has much better electrochemical stability even in anodic oxidation conditions [29,48,49]. The degradation rate of Ir-g-CN is only 0.45 and 0.87 mV h^{-1} in 0.5 M H_2SO_4 and 1.0 M KOH, respectively, and that of Ru-g-CN is 0.66 and 1.11 mV h^{-1} , both lower than that of the commercial Pt/C benchmark (0.96 and 1.58 mV h^{-1}).

3.4. Photocatalytic performance of Ir-g-CN and Ru-g-CN

Besides electrocatalytic performance, the photocatalytic H_2 evolution performance of Ir-g-CN and Ru-g-CN was also investigated in a suspension system, given that g-CN itself is a photocatalyst with a suitable bandgap for visible light water splitting [10,50]. According to the photocatalytic tests (Fig. 5a), where methanol was used as the sacrificial agent, the pristine g-CN exhibits an H_2 production rate of 58 $\mu\text{mol H}_2 \text{ g}_{\text{catalyst}}^{-1} \text{ h}^{-1}$, similar to and even higher than that in some previous reports on g-CN [11,51,52]. According to the DR UV-vis and PL results discussed above (Fig. 3a and b), this relatively low H_2 evolution rate might result from rapid recombination of photo-generated charge carriers. Once Ir or Ru single-atoms are loaded as the co-catalysts, even only with an ultralow loading mass (1.71 wt% for Ir-g-CN and 0.24 wt% for Ru-g-CN), significant enhancement in the H_2 production rate has been observed, amounting to 2122 $\mu\text{mol H}_2 \text{ g}_{\text{catalyst}}^{-1} \text{ h}^{-1}$ for Ir-g-CN and 1175 $\mu\text{mol H}_2 \text{ g}_{\text{catalyst}}^{-1} \text{ h}^{-1}$ for Ru-g-CN, much higher than that of atomic palladium on g-CN (728 $\mu\text{mol H}_2 \text{ g}_{\text{catalyst}}^{-1} \text{ h}^{-1}$) [24], $\text{g-C}_3\text{N}_4\text{-Pt}^{2+}$ (605 $\mu\text{mol H}_2 \text{ g}_{\text{catalyst}}^{-1} \text{ h}^{-1}$) [41], and 3Ru/TiO_2 (1000 $\mu\text{mol H}_2 \text{ g}_{\text{catalyst}}^{-1} \text{ h}^{-1}$) [53]. If only normalized to the mass and mole of

noble metals, the Ru-g-CN catalyst shows a remarkably high photocatalytic H_2 production rate of 489.7 $\text{mmol H}_2 \text{ g}_{\text{Ru}}^{-1} \text{ h}^{-1}$ or a photocatalytic TOF value of 50.4 h^{-1} (Fig. 5b and c), greater than that of Ir-g-CN (124.1 $\text{mmol H}_2 \text{ g}_{\text{Ir}}^{-1} \text{ h}^{-1}$, TOF: 25.2 h^{-1}) and other Ru-based photocatalysts (Table S6), due likely to the ultralow loading of Ru (0.24 wt%) on g-CN. The photocatalytic stability and re-usability of Ir-g-CN and Ru-g-CN catalysts were further examined by repeating the photocatalytic reaction cycles. The H_2 evolution rate of both catalysts remained constant during the tests for at least three cycles (Fig. 5d), illustrating their good stability and re-usability.

3.5. Theoretical insight into the enhanced electrocatalytic and photocatalytic HER performance

To gain further insights into the markedly enhanced electrocatalytic and photocatalytic performance of Ir-g-CN and Ru-g-CN with respect to the pristine g-CN, we performed DFT calculations. The proposed atomic models of the pristine g-CN, Ir-g-CN and Ru-g-CN catalysts are illustrated in Fig. S13. As shown in Fig. 6a, the g-CN has an indirect bandgap of 2.7 eV, which is in good agreement with our experimental data (Fig. 3a) and previous reports [17,18]. According to the optimal models we obtained (Fig. S13), introducing Ir or Ru single-atoms onto g-CN dramatically changes the electronic structure of the resulting Ir-g-CN and Ru-g-CN (Fig. 6a and b), which show significantly reduced bandgaps and increased projected density of states (PDOS) near the Fermi level. Such modification may result in a higher carrier density and facilitate the charge transfer on and near the surface [20,54], where the electrocatalytic and photocatalytic reactions are taking place, eventually enhancing the electrocatalytic and photocatalytic activity. Note that the theoretically calculated bandgaps of Ir-g-CN and Ru-g-CN are smaller than the experimentally measured (Fig. 3), owing to the fact that the Ir/Ru density on g-CN in our models (34.3 wt% for Ir-g-CN and

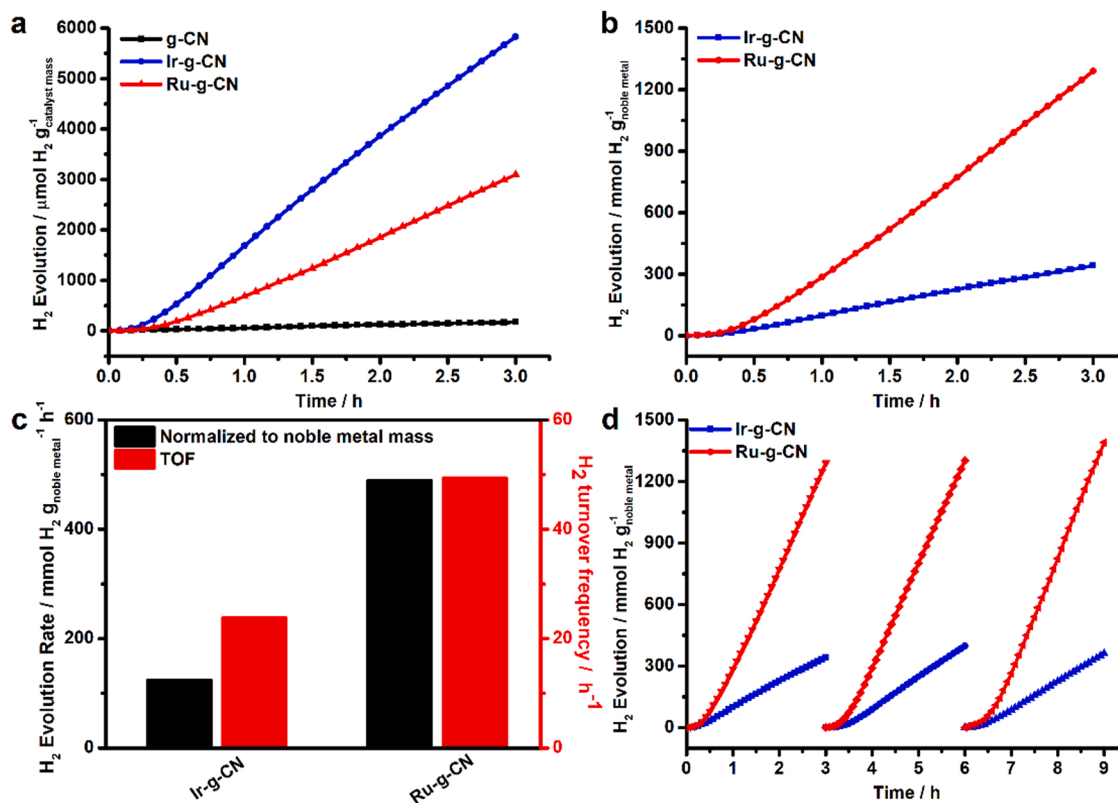


Fig. 5. Photocatalytic H_2 evolution tests of pristine g-CN, Ir-g-CN and Ru-g-CN catalysts. (a) H_2 evolution normalized to the catalyst mass vs. photocatalytic reaction duration. (b) H_2 evolution normalized only to the mass of noble metal vs. photocatalytic reaction duration. (c) Comparison of mass-based hydrogen evolution rate and the TOF values. (d) Photocatalytic test cycles of Ir-g-CN and Ru-g-CN under light irradiation.

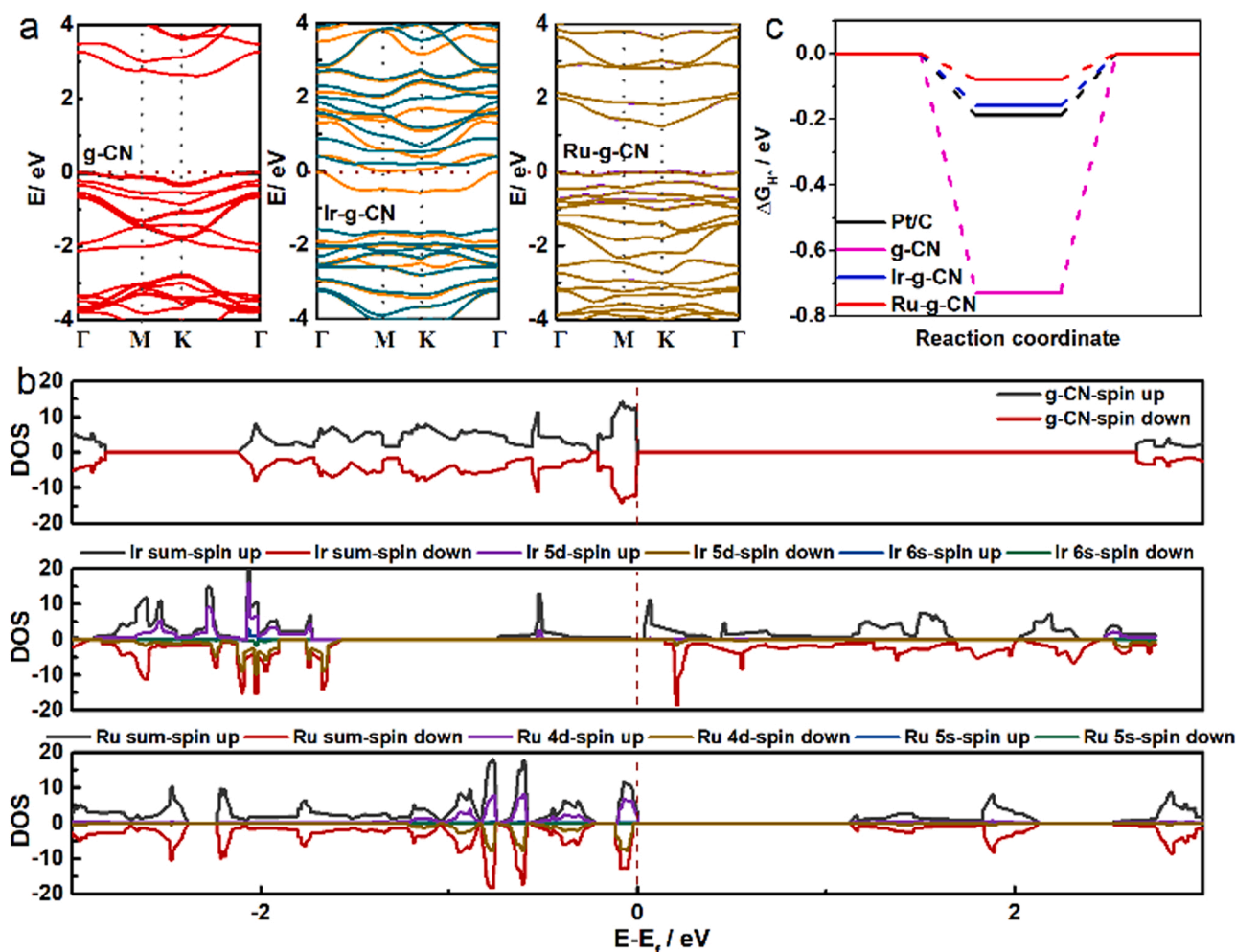


Fig. 6. (a) Energy band structures, (b) Projected density of states, and (c) The Gibbs free-energy diagram towards the HER of the pristine g-CN, Ir-g-CN and Ru-g-CN catalysts.

21.6 wt% for Ru-g-CN) is much higher than the measured Ir/Ru loading density (1.71 wt% for Ir-g-CN and 0.24 wt% for Ru-g-CN). Nevertheless, it is unambiguous that loading single-atoms on g-CN can decrease the bandgap, and this has been confirmed by other groups as well [17,18].

Furthermore, the Gibbs free energy (ΔG_{H}) diagrams of pristine g-CN, Ir-g-CN and Ru-g-CN catalysts for the HER were calculated (Fig. 6c). The ΔG_{H} of hydrogen adsorption has been proposed to be a suitable descriptor of the HER activity, and the closer ΔG_{H} value is to zero, the better the HER activity. According to Fig. 6c, Ru-g-CN exhibits a ΔG_{H} value (-0.08 eV) much closer to zero than Ir-g-CN (-0.16 eV), Pt (111) surface (-0.19 eV) and g-CN (-0.73 eV). This indicates that the Ru sites in Ru-g-CN provide optimal adsorption for H^* intermediates, compared to the Ir-g-CN and Pt/C controls, which rationally explains the intrinsically high specific activity of Ru-g-CN (Fig. S10). Overall, our DFT calculations consistently support the experimental results, demonstrating that introducing Ir and Ru atoms onto the g-CN support alters the electronic structures and results in remarkably improved electrocatalytic and photocatalytic HER activity.

4. Conclusions

In summary, we synthesized single-atom Ir and Ru catalysts supported on mesoporous graphitic carbon nitride, which can act as efficient and stable HER catalysts for electrocatalytic and photocatalytic water splitting. In particular, Ru-g-CN shows outstanding electrocatalytic performance in terms of specific activity, mass activity, and

catalytic stability. It exhibits a high TOF value of 12.9 and 5.1 s^{-1} at $\eta = 100 \text{ mV}$ in $0.5 \text{ M H}_2\text{SO}_4$ and 1.0 M KOH , respectively, which outperforms Ir-g-CN, commercial Pt/C benchmark and many other advanced HER catalysts recently reported in the literature. In addition, Ru-g-CN affords an exceptionally high mass activity of 24.55 and 8.78 A mg^{-1} at $\eta = 100 \text{ mV}$ in acidic and alkaline solutions, meanwhile exhibiting a high apparent current density, which is favorable for practical applications. Impressively, Ru-g-CN also reveals outstanding photocatalytic HER activity showing a high H_2 production rate of $489.7 \text{ mmol H}_2 \text{ g}_{\text{Ru}}^{-1} \text{ h}^{-1}$, along with good catalytic stability. For single-atom catalysts with a low metal loading density, the catalytic performance should be comprehensively assessed in the context of practical application. The mass activity alone should not be overemphasized without considering the catalyst's apparent activity. To this end, our Ru-g-CN catalysts exhibit a high mass activity, and at the same time, a high apparent activity. All in all, our experimental results are supported by the theoretical calculations, in which introducing Ir or Ru onto the surface of g-CN has been demonstrated to be able to promote the electron transfer and lead to optimal Gibbs free energy of hydrogen adsorption, contributing to the remarkable improvement of the electrocatalytic and photocatalytic HER performance.

CRediT authorship contribution statement

Z.P.Y. and L.L. conceived the experiments; Z.P.Y. performed XRD, SEM, XPS, electrocatalytic/photocatalytic tests and wrote the initial

manuscript; Y.F.L. performed DFT calculations; A.T-P. synthesized the g-CN support and did the DR UV-vis and PL measurements; V.M.D and L.S. performed XANES and EXAFS experiments and contributed to data analysis; A.P.L. carried out TEM characterization; O.B. contributed to XPS and UPS measurements; M.J.S. performed the nitrogen adsorption/desorption porosimetry measurements; I.A., A.A., A.M.T.S. and C.G.S. contributed to the discussion. J.L.F. and L.L. contributed to data analyses and wrote the final manuscript. All authors read and agreed on the manuscript. J.L.F. and L.L. coordinated the project.

Declaration of Competing Interest

The authors declare that they have no known competing financial interests or personal relationships that could have appeared to influence the work reported in this paper.

Acknowledgments

L.L. acknowledges the financial support from the National Innovation Agency of Portugal through the Mobilizador project (Baterias 2030, Grant no. POCI-01-0247-FEDER-046109). Z.P.Y. is grateful for the scholarship offered by the China Scholarship Council (Grant no. 201806150015). A.T-P. acknowledges Fundação para a Ciência e a Tecnologia (FCT) for his scholarship SFRH/BD/143487/2019. This work was also partially funded by European Regional Development Fund (ERDF) through COMPETE2020 program and by FCT through the MicrophotOGEN project (POCI-01-0145-FEDER-030674), as well as supported by LA/P/0045/2020 (ALiCE), UIDB/50020/2020 and UIDP/50020/2020 (LSRE-LCM), funded by national funds through FCT/MCTES (PIDDAC). This work was carried out in part through the use of the INL Advanced Electron Microscopy, Imaging and Spectroscopy Facility. The XAS experiments were performed at the CLAES beamline, ALBA Synchrotron.

Appendix A. Supporting information

Supplementary data associated with this article can be found in the online version at [doi:10.1016/j.apcatb.2022.121318](https://doi.org/10.1016/j.apcatb.2022.121318).

References

- [1] M. De Simón-Martín, B.-R. Cortes-Nava, R. Rodríguez-Parra, F. Carro-De Lorenzo, The role of green hydrogen in the energy transition of the industry, *DYNA* 96 (2021) 200–206.
- [2] S. Furfari, A. Clerici, Green hydrogen: the crucial performance of electrolyzers fed by variable and intermittent renewable electricity, *Eur. Phys. J.* 136 (2021) 509.
- [3] L. Liu, Platinum group metal free nano-catalysts for proton exchange membrane water electrolysis, *Curr. Opin. Chem. Eng.* 34 (2021), 100743.
- [4] J. Xu, I. Amorim, Y. Li, J. Li, Z. Yu, B. Zhang, A. Araujo, N. Zhang, L. Liu, Stable overall water splitting in an asymmetric acid/alkaline electrolyzer comprising a bipolar membrane sandwiched by bifunctional cobalt-nickel phosphide nanowire electrodes, *Carbon Energy* 2 (2020) 646–655.
- [5] S.J. Mun, S.-J. Park, Graphitic carbon nitride materials for photocatalytic hydrogen production via water splitting: a short review, *Catalysts* 9 (2019) 805.
- [6] X. Xiao, L. Zhang, H. Meng, B. Jiang, H. Fu, Single metal atom decorated carbon nitride for efficient photocatalysis: synthesis, structure, and applications, *Sol. RRL* 5 (2021), 2000609.
- [7] M.G. Walter, E.L. Warren, J.R. McKone, S.W. Boettcher, Q. Mi, E.A. Santori, N. S. Lewis, Solar water splitting cells, *Chem. Rev.* 110 (2010) 6446–6473.
- [8] S.M. Thalluri, L. Bai, C. Lv, Z. Huang, X. Hu, L. Liu, Strategies for semiconductor/electrocatalyst coupling toward solar-driven water splitting, *Adv. Sci.* 7 (2020), 1902102.
- [9] X. Wang, K. Maeda, A. Thomas, K. Takanebe, G. Xin, J.M. Carlsson, K. Domen, M. Antonietti, A metal-free polymeric photocatalyst for hydrogen production from water under visible light, *Nat. Mater.* 8 (2009) 76–80.
- [10] M.S. Nasir, G. Yang, I. Ayub, S. Wang, L. Wang, X. Wang, W. Yan, S. Peng, S. Ramakrishna, Recent development in graphitic carbon nitride based photocatalysis for hydrogen generation, *Appl. Catal. B Environ.* 257 (2019), 117855.
- [11] W. Li, X.-s. Chu, F. Wang, Y.-y. Dang, X.-y. Liu, X.-c. Wang, C.-y. Wang, Enhanced cocatalyst-support interaction and promoted electron transfer of 3D porous g-C₃N₄/GO-M (Au, Pd, Pt) composite catalysts for hydrogen evolution, *Appl. Catal. B Environ.* 288 (2021), 120034.
- [12] X. Li, W. Bi, L. Zhang, S. Tao, W. Chu, Q. Zhang, Y. Luo, C. Wu, Y. Xie, Single-atom Pt as Co-catalyst for enhanced photocatalytic H₂ evolution, *Adv. Mater.* 28 (2016) 2427–2431.
- [13] W. Niu, Y. Yang, Graphitic carbon nitride for electrochemical energy conversion and storage, *ACS Energy Lett.* 3 (2018) 2796–2815.
- [14] Y. Yang, J. Kim, C. Kim, A. Seong, O. Kwon, J.H. Lee, I. Kristanto, L. Zhang, J. Zhou, J.-Q. Wang, J.-B. Baek, S.K. Kwak, G. Kim, Edge-selective decoration with ruthenium at graphitic nanoplatelets for efficient hydrogen production at universal pH, *Nano Energy* 76 (2020), 105114.
- [15] Y. Zheng, Y. Jiao, Y. Zhu, L.H. Li, Y. Han, Y. Chen, M. Jaroniec, S.-Z. Qiao, High electrocatalytic hydrogen evolution activity of an anomalous ruthenium catalyst, *J. Am. Chem. Soc.* 138 (2016) 16174–16181.
- [16] J. Mahmood, F. Li, S.-M. Jung, M.S. Okyay, I. Ahmad, S.-J. Kim, N. Park, H. Y. Jeong, J.-B. Baek, An efficient and pH-universal ruthenium-based catalyst for the hydrogen evolution reaction, *Nat. Nanotechnol.* 12 (2017) 441–446.
- [17] T. Tong, B. He, B. Zhu, B. Cheng, L. Zhang, First-principle investigation on charge carrier transfer in transition-metal single atoms loaded g-C₃N₄, *Appl. Surf. Sci.* 459 (2018) 385–392.
- [18] T. Tong, B. Zhu, C. Jiang, B. Cheng, J. Yu, Mechanistic insight into the enhanced photocatalytic activity of single-atom Pt, Pd or Au-embedded g-C₃N₄, *Appl. Surf. Sci.* 433 (2018) 1175–1183.
- [19] J. Fu, S. Wang, Z. Wang, K. Liu, H. Li, H. Liu, J. Hu, X. Xu, H. Li, M. Liu, Graphitic carbon nitride based single-atom photocatalysts, *Front. Phys.* 15 (2020) 33201.
- [20] X.-H. Jiang, L.-S. Zhang, H.-Y. Liu, D.-S. Wu, F.-Y. Wu, L. Tian, L.-L. Liu, J.-P. Zou, S.-L. Luo, B.-B. Chen, Silver single atom in carbon nitride catalyst for highly efficient photocatalytic hydrogen evolution, *Angew. Chem. Int. Ed.* 59 (2020) 23112–23116.
- [21] Z. Yu, J. Xu, S. Feng, X. Song, O. Bondarchuk, J.L. Faria, Y. Ding, L. Liu, Rhodium single-atom catalysts with enhanced electrocatalytic hydrogen evolution performance, *New J. Chem.* 45 (2021) 5770–5774.
- [22] P. Zhou, F. Lv, N. Li, Y. Zhang, Z. Mu, Y. Tang, J. Lai, Y. Chao, M. Luo, F. Lin, J. Zhou, D. Su, S. Guo, Strengthening reactive metal-support interaction to stabilize high-density Pt single atoms on electron-deficient g-C₃N₄ for boosting photocatalytic H₂ production, *Nano Energy* 56 (2019) 127–137.
- [23] Y. Peng, B. Lu, L. Chen, N. Wang, J.E. Lu, Y. Ping, S. Chen, Hydrogen evolution reaction catalyzed by ruthenium ion-complexed graphitic carbon nitride nanosheets, *J. Mater. Chem. A* 5 (2017) 18261–18269.
- [24] L. Liu, X. Wu, L. Wang, X. Xu, L. Gan, Z. Si, J. Li, Q. Zhang, Y. Liu, Y. Zhao, R. Ran, X. Wu, D. Weng, F. Kang, Atomic palladium on graphitic carbon nitride as a hydrogen evolution catalyst under visible light irradiation, *Commun. Chem.* 2 (2019) 18.
- [25] A. Torres-Pinto, M.J. Sampaio, C.G. Silva, J.L. Faria, A.M.T. Silva, Metal-free carbon nitride photocatalysis with in situ hydrogen peroxide generation for the degradation of aromatic compounds, *Appl. Catal. B Environ.* 252 (2019) 128–137.
- [26] L. Simonelli, C. Marini, W. Olszewski, M. Ávila Pérez, N. Ramanan, G. Guilera, V. Cuartero, K. Klementiev, CLAES: the hard X-ray absorption beamline of the ALBA CELLS synchrotron, *Cogent Phys.* 3 (2016), 1231987.
- [27] B. Ravel, M. Newville, ATHENA, ARTEMIS, HEPHAESTUS: data analysis for X-ray absorption spectroscopy using IFEFFIT, *J. Synchrotron Radiat.* 12 (2005) 537–541.
- [28] C.C.L. McCrory, S. Jung, J.C. Peters, T.F. Jaramillo, Benchmarking heterogeneous electrocatalysts for the oxygen evolution reaction, *J. Am. Chem. Soc.* 135 (2013) 16977–16987.
- [29] J. Xu, J. Li, Z. Lian, A. Araujo, Y. Li, B. Wei, Z. Yu, O. Bondarchuk, I. Amorim, V. Tileli, B. Li, L. Liu, Atomic-step enriched ruthenium-iridium nanocrystals anchored homogeneously on mof-derived support for efficient and stable oxygen evolution in acidic and neutral media, *ACS Catal.* 11 (2021) 3402–3413.
- [30] I. Amorim, J. Xu, N. Zhang, Z. Yu, A. Araújo, F. Bento, L. Liu, Dual-phase CoP-CoTe₂ nanowires as an efficient bifunctional electrocatalyst for bipolar membrane-assisted acid-alkaline water splitting, *Chem. Eng. J.* 420 (2021), 130454.
- [31] G. Kresse, J. Furthmüller, Efficient iterative schemes for ab initio total-energy calculations using a plane-wave basis set, *Phys. Rev. B* 54 (1996) 11169–11186.
- [32] P.E. Blöchl, Projector augmented-wave method, *Phys. Rev. B* 50 (1994) 17953–17979.
- [33] J.P. Perdew, K. Burke, M. Ernzerhof, Generalized gradient approximation made simple, *Phys. Rev. Lett.* 77 (1996) 3865–3868.
- [34] J. Heyd, G.E. Scuseria, M. Ernzerhof, Hybrid functionals based on a screened Coulomb potential, *J. Chem. Phys.* 118 (2003) 8207–8215.
- [35] A. Walcarius, Mesoporous materials and electrochemistry, *Chem. Soc. Rev.* 42 (2013) 4098–4140.
- [36] J. Feng, H. Gao, L. Zheng, Z. Chen, S. Zeng, C. Jiang, H. Dong, L. Liu, S. Zhang, X. Zhang, A Mn-N₃ single-atom catalyst embedded in graphitic carbon nitride for efficient CO₂ electroreduction, *Nat. Commun.* 11 (2020) 4341.
- [37] P. Yang, S. Zuo, F. Zhang, B. Yu, S. Guo, X. Yu, Y. Zhao, J. Zhang, Z. Liu, Carbon nitride-based single-atom Cu catalysts for highly efficient carboxylation of alkynes with atmospheric CO₂, *Ind. Eng. Chem. Res.* 59 (2020) 7327–7335.
- [38] M.J. Lima, A.M.T. Silva, C.G. Silva, J.L. Faria, Graphitic carbon nitride modified by thermal, chemical and mechanical processes as metal-free photocatalyst for the selective synthesis of benzaldehyde from benzyl alcohol, *J. Catal.* 353 (2017) 44–53.
- [39] L. Bai, Z. Duan, X. Wen, R. Si, Q. Zhang, J. Guan, Highly dispersed ruthenium-based multifunctional electrocatalyst, *ACS Catal.* 9 (2019) 9897–9904.
- [40] Z. Li, Y. Chen, S. Ji, Y. Tang, W. Chen, A. Li, J. Zhao, Y. Xiong, Y. Wu, Y. Gong, T. Yao, W. Liu, L. Zheng, J. Dong, Y. Wang, Z. Zhuang, W. Xing, C.-T. He, C. Peng, W.-C. Cheong, Q. Li, M. Zhang, Z. Chen, N. Fu, X. Gao, W. Zhu, J. Wan, J. Zhang, L. Gu, S. Wei, P. Hu, J. Luo, J. Li, C. Chen, Q. Peng, X. Duan, Y. Huang, X.-M. Chen,

- D. Wang, Y. Li, Iridium single-atom catalyst on nitrogen-doped carbon for formic acid oxidation synthesized using a general host–guest strategy, *Nat. Chem.* 12 (2020) 764–772.
- [41] Y. Li, Z. Wang, T. Xia, H. Ju, K. Zhang, R. Long, Q. Xu, C. Wang, L. Song, J. Zhu, J. Jiang, Y. Xiong, Implementing metal-to-ligand charge transfer in organic semiconductor for improved visible-near-infrared photocatalysis, *Adv. Mater.* 28 (2016) 6959–6965.
- [42] W. Luo, Y. Li, J. Wang, J. Liu, N. Zhang, M. Zhao, J. Wu, W. Zhou, L. Wang, Asymmetric structure engineering of polymeric carbon nitride for visible-light-driven reduction reactions, *Nano Energy* 87 (2021), 106168.
- [43] D. Zhu, Q. Zhou, Nitrogen doped g-C₃N₄ with the extremely narrow band gap for excellent photocatalytic activities under visible light, *Appl. Catal. B Environ.* 281 (2021), 119474.
- [44] J.N. Hansen, H. Prats, K.K. Toudahl, N. Mørch Secher, K. Chan, J. Kibsgaard, I. Chorkendorff, Is there anything better than Pt for HER? *ACS Energy Lett.* 6 (2021) 1175–1180.
- [45] J. Xu, T. Liu, J. Li, B. Li, Y. Liu, B. Zhang, D. Xiong, I. Amorim, W. Li, L. Liu, Boosting the hydrogen evolution performance of ruthenium clusters through synergistic coupling with cobalt phosphide, *Energy Environ. Sci.* 11 (2018) 1819–1827.
- [46] Q. Wu, M. Luo, J. Han, W. Peng, Y. Zhao, D. Chen, M. Peng, J. Liu, F.M.F. de Groot, Y. Tan, Identifying electrocatalytic sites of the nanoporous copper–ruthenium alloy for hydrogen evolution reaction in alkaline electrolyte, *ACS Energy Lett.* 5 (2020) 192–199.
- [47] Z. Pu, I.S. Amiinu, Z. Kou, W. Li, S. Mu, RuP₂-based catalysts with platinum-like activity and higher durability for the hydrogen evolution reaction at all pH values, *Angew. Chem. Int. Ed.* 56 (2017) 11559–11564.
- [48] J. Yang, W. Li, D. Wang, Y. Li, Electronic metal–support interaction of single-atom catalysts and applications in electrocatalysis, *Adv. Mater.* 32 (2020), 2003300.
- [49] J. Yang, B. Chen, X. Liu, W. Liu, Z. Li, J. Dong, W. Chen, W. Yan, T. Yao, X. Duan, Y. Wu, Y. Li, Efficient and robust hydrogen evolution: phosphorus nitride imide nanotubes as supports for anchoring single ruthenium sites, *Angew. Chem. Int. Ed.* 57 (2018) 9495–9500.
- [50] I.F. Teixeira, E.C.M. Barbosa, S.C.E. Tsang, P.H.C. Camargo, Carbon nitrides and metal nanoparticles: from controlled synthesis to design principles for improved photocatalysis, *Chem. Soc. Rev.* 47 (2018) 7783–7817.
- [51] S. Gao, X. Wang, C. Song, S. Zhou, F. Yang, Y. Kong, Engineering carbon-defects on ultrathin g-C₃N₄ allows one-pot output and dramatically boosts photoredox catalytic activity, *Appl. Catal. B Environ.* 295 (2021), 120272.
- [52] L. Zhang, R. Long, Y. Zhang, D. Duan, Y. Xiong, Y. Zhang, Y. Bi, Direct observation of dynamic bond evolution in single-atom Pt/C₃N₄ catalysts, *Angew. Chem. Int. Ed.* 59 (2020) 6224–6229.
- [53] W. Ouyang, M.J. Muñoz-Batista, A. Kubacka, R. Luque, M. Fernández-García, Enhancing photocatalytic performance of TiO₂ in H₂ evolution via Ru co-catalyst deposition, *Appl. Catal. B Environ.* 238 (2018) 434–443.
- [54] D. Zhao, C.-L. Dong, B. Wang, C. Chen, Y.-C. Huang, Z. Diao, S. Li, L. Guo, S. Shen, Synergy of dopants and defects in graphitic carbon nitride with exceptionally modulated band structures for efficient photocatalytic oxygen evolution, *Adv. Mater.* 31 (2019), 1903545.